



Characteristic Curves of Polar Fluids: (II) The Two-Center Lennard–Jones Plus Quadrupole Fluid

Hans Renneis¹ · Simon Stephan¹

Received: 16 March 2024 / Accepted: 31 March 2024
© The Author(s) 2024

Abstract

A systematic study of *Brown's* characteristic curves of the two center Lennard–Jones plus point quadrupole (2CLJQ) fluid was carried out using molecular simulation and molecular-based equation of state (EOS) modeling. The model parameters (elongation and quadrupole moment) were varied systematically covering the range relevant for real fluid models. In total, 36 model fluids were studied. The independent predictions from the EOS and the computer experiments are found to be in very good agreement. Based on these results, the influence of the quadrupole moment on the fluid behavior at extreme conditions is elucidated. The quadrupole interactions are found to have a surprisingly minor influence on the extreme state fluid behavior. In particular, for the Amagat curve, the quadrupole moment is found to have an almost negligible influence in a wide temperature range. The results also provide new insights into the applicability of the corresponding states principle, which is compared to other molecular property features. Interestingly, for a wide range of quadrupole moments, the fluid behavior at extreme conditions is conform with the corresponding states principle—opposite to the influence of other molecular features. This is attributed to the symmetry of the quadrupole interactions. Moreover, an empirical correlation for the characteristic curves was developed as a global function of the model parameters and tested on real substance models. Additionally, the applicability of *Batschinski's* linearity law for the Zeno curve was assessed using the results for the 2CLJQ fluid.

Keywords *Brown's* characteristic curves · Equation of state · Molecular dynamics simulation · Polar interactions

✉ Simon Stephan
simon.stephan@rptu.de

¹ Laboratory of Engineering Thermodynamics (LTD), RPTU Kaiserslautern, Erwin-Schrödinge-Straße 44, 67663 Kaiserslautern, Germany

1 Introduction

Polarities play an important role for many real fluids, which can be favorably modeled using multipole expansions [1, 2], i.e. dipoles, quadrupoles, octopoles, etc. For molecular models, in particular dipoles and quadrupoles are frequently used. A quadrupole describes the electrostatic field of four point charges of the same magnitude. A linear point quadrupole describes the electrostatic field of three point charges with q , $-2q$, q , which corresponds to two collinear point dipoles with the same magnitude, but opposite orientation. Hence, a point quadrupole describes a relatively complex charge distribution considering the fact that it is represented by a single interaction site. The two-center Lennard–Jones plus quadrupole fluid (2CLJQ) is an important model class that comprises a point quadrupole. This model class is often used for the description of real substances, e.g. halogens, simple gases, and refrigerants [3–10]. In the 2CLJQ model class, two identical Lennard–Jones interaction sites with the dispersion energy ϵ , the size parameter σ , and the mass M are placed at an elongation distance L . Additionally, a point quadrupole is positioned at the center of the two Lennard–Jones sites and its orientation is aligned with the molecule axis.

The 2CLJQ model fluid has been systematically studied in the literature for several thermophysical properties, e.g. vapor–liquid equilibria [11], interfacial properties [12–14], and virial coefficients [15, 16]. Also, several Helmholtz energy models have been proposed for modeling the effect of quadrupole interactions on thermodynamic properties [17–19]. Thereby, the influence of molecular interaction quadrupole moments on different macroscopic properties has been elucidated. Yet, homogeneous state properties of the 2CLJQ model fluid have not been addressed as systematically—especially at extreme conditions. The behavior of fluids at high pressure and temperature is relevant for several areas of science and technology, e.g. tribology [20–22], astronomy [23, 24], and geology [25, 26].

An interesting approach to study the properties of fluids at extreme conditions are *Brown's* characteristic curves, i.e. the Zeno, Amagat, Boyle, and Charles curve [27]. These characteristic curves span a wide range of thermodynamic states. A detailed discussion of the properties of the characteristic curves can be found in Refs. [27, 28, 30]. The four curves were postulated to have specific properties [27]. This has been used for testing the extrapolation behavior of equation of state (EOS) models and eventually uncovering artifacts [29–40]. In this work, the 2CLJQ model class is used to study the influence of quadrupole interactions on *Brown's* characteristic curves using first principle molecular simulations and EOS modeling. Among the characteristic curves, the Charles curve, also known as the Joule–Thomson inversion curve, plays a particular important technical role as it defines the locus of state points defining the transition from a temperature increase or decrease upon isenthalpic throttling, which is particularly relevant for refrigerants. Since there is little experimental data for the Charles curve (and the other characteristic curves) available, often molecular-based methods are used for their modeling [28, 41–43]. Numerous studies have investigated the Charles curve for refrigerant substances using molecular simulation [44–50]. In this work, we

also apply the results from the 2CLJQ model class for the characteristic curves to real substances—in particular refrigerants.

In a previous work of our group, we studied *Brown's* characteristic curves of the two center Lennard–Jones plus dipole (2CLJD) model class [51], which gave first time insights into the effect of polar interactions, namely dipoles on the topology of *Brown's* characteristic curves. In this work, a systematic study of the characteristic curves of quadrupolar fluids is carried out. In the literature, *Brown's* characteristic curves were also studied for other fluid classes such as Mie fluids [29], the Lennard–Jones fluid [28, 39], and selected real substances [28, 40, 52]. Important differences were reported for the influence of different molecular properties on the characteristic curves, e.g. the repulsive and dispersive exponent of the Mie potential and the dipole moment [29, 51]. The results from this work for the 2CLJQ fluids are put in context with those results from the literature, which provides interesting insights in the differences of the influence of the molecular interaction mechanisms on the fluid behavior at extreme conditions.

A peculiarity of the characteristic curves—especially for the Zeno curve—is *Batschinski's* linearity law [53]. It states that the Zeno curve exhibits a linear shape in the density-temperature plane ($\rho - T$)—starting at the Boyle temperature in the zero-density limit. *Batschinski* derived this linear dependency solely from the van der Waals equation and thermodynamic principles. This linearity of the Zeno curve, often referred to as the ideal-gas curve, unit compressibility line, or orthometric line, has been studied for both real substance and model fluids [54–56]. As experimental data for the Zeno curve is practically not available, mostly EOS models are used for studying the linearity law for different types of fluids. In this work, we use the first principle molecular simulation results for the 2CLJQ fluid to assess the applicability of *Batschinski's* linearity law for this model class.

Brown's characteristic curves are, moreover, well-suited to investigate the corresponding states law and its applicability at high temperature and pressure. The principle of corresponding states, originally formulated by Pitzer [57] and Guggenheim [58], states that substances share identical reduced states with respect to their critical properties. Also for the corresponding states law derivation, originally, simple fluids were considered and it was early recognized that more complex molecular interactions can cause deviations from the corresponding states law [58, 59]. However, the effects of different specific interaction types on these deviations have not been fully understood yet. In this work, we use the characteristic curves of the 2CLJQ fluids to assess the applicability of the corresponding states law at extreme conditions for this model class (and compare those to results for other molecular interaction features). The principle of corresponding states was tested for different thermophysical properties of the 2CLJQ fluid class previously. The corresponding states applicability has been studied for the second virial coefficient [58, 60], for vapor–liquid equilibrium properties [11, 58, 61, 62], and for interfacial properties [63–65]. However, the applicability of the corresponding states law to homogeneous state property behavior at extreme conditions was not studied yet to the best of our knowledge.

This work is outlined as follows: First, the 2CLJQ model fluid class is briefly introduced. Then, the employed methods are introduced, namely the molecular simulation methodology and the EOS modeling. In the results section, first, the

zero-density limit data of the characteristic curves are presented and discussed. Then, the results for the entire characteristic curves as obtained from molecular simulation are compared to the EOS predictions for selected 2CLJQ fluids. Also, the results for the applicability of the corresponding states law and *Batschinski's* linearity law are presented and discussed. Then, the atomistic structure of fluid state points along the characteristic curves is discussed. Finally, conclusions are drawn.

2 Investigated Fluids

The intermolecular potential of the 2CLJQ fluid can be written as

$$u_{2CLJQ}(r_{ij}, \omega_i, \omega_j, L, Q^2) = u_{2CLJ}(r_{ij}, \omega_i, \omega_j, L) + u_Q(r_{ij}, \omega_i, \omega_j, Q^2), \quad (1)$$

with u_{2CLJ} being the potential of the two-center Lennard–Jones model and u_Q being the point quadrupole contribution. The expression for the interaction potential of the 2CLJ model can be written as

$$u_{2CLJ}(r_{ij}, \omega_i, \omega_j, L) = \sum_{a=1}^2 \sum_{b=1}^2 4\epsilon \left[\left(\frac{\sigma}{r_{ab}} \right)^{12} - \left(\frac{\sigma}{r_{ab}} \right)^6 \right], \quad (2)$$

where the parameters σ and ϵ are the size and the energy parameter of the Lennard–Jones potential [66], respectively. The distance between two interaction sites is denoted by r . The point quadrupole interaction potential can be written as

$$u_Q(r_{ij}, \omega_i, \omega_j, Q^2) = \frac{1}{4\pi\epsilon_0} \frac{3}{4} \frac{Q^2}{|r_{ij}|^5} f(\omega), \quad (3)$$

where ω_i and ω_j indicate the orientations of two molecules i and j and $f(\omega)$ is a dimensionless expression depending on the angle between these two molecules [1].

In this work, we study symmetric 2CLJQ fluids, i.e. both Lennard–Jones sites have identical ϵ , σ , and mass M . The point quadrupole moment is aligned along the axis connecting the two LJ sites. Using the Lennard–Jones units system [67], the 2CLJQ model class is a two-parameter system, namely the elongation L/σ and the (squared) quadrupole moment $Q^2/(4\pi\epsilon_0\epsilon\sigma^5)$, with ϵ_0 being the permittivity of vacuum. For simplicity, we adopted the convention $4\pi\epsilon_0 = 1$. Accordingly, the results for the 2CLJQ model fluids are presented using the Lennard–Jones units system.

Our study comprises a total of 36 2CLJQ fluids. These fluids cover a broad range of L and Q values relevant for real substance models available in the literature [3–8]. The 2CLJQ parameters were varied in this work in the range $L/\sigma = 0, 0.2, 0.4, 0.505, 0.6, 0.8, 1$ and $Q^2/\epsilon\sigma^5 = 1, 2, 3, 4, 5$. Figure 1 shows the studied parameter range of 2CLJQ fluids in comparison to real substance model parameters from the literature. The model fluids characterized by $L/\sigma = 0$ comprise two overlapping Lennard–Jones interaction sites.

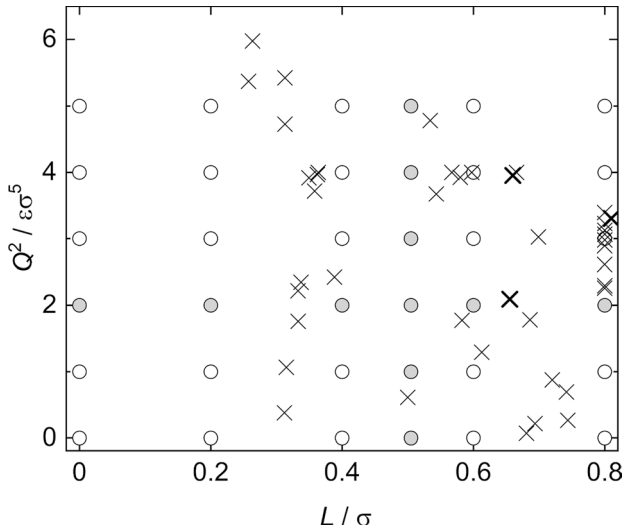


Fig. 1 Parameters for the 2CLJQ model class: The model fluids investigated in this work are represented by circles. Filled circles indicate fluids focused on in the results section. Crosses represent real substance model parameters taken from the literature [3–9, 68]. Thick crosses indicate real substance molecular models discussed below

3 Methods

The methodology follows that of the first part [51]: *Brown's* characteristic curves were determined using the molecular simulation method from Ref. [52] and a molecular-based EOS. Additionally, an empirical correlation of the molecular simulation results was developed. The simulations were carried out with the code *ms2* [69, 70]. For the EOS, Helmholtz energy terms proposed by Lísal et al. [71] and Gross [17] were used.

The EOS used in this work is a perturbation type framework modeling the reduced Helmholtz energy per particle $\tilde{a} = a/k_B T$ as a function of the density ρ and temperature T as well as of the model parameters L and Q . The model comprises a term for the dispersive and repulsive interactions of the two Lennard–Jones sites \tilde{a}_{2CLJ} that was adopted from Lísal et al. [71] and a term for the quadrupole interactions \tilde{a}_Q that was adopted from Gross [17]. The model can be written as

$$\tilde{a}(T, \rho, L, Q) = \tilde{a}_{2CLJ}(T, \rho, L) + \tilde{a}_Q(T, \rho, Q). \quad (4)$$

This EOS model was used for computing *Brown's* characteristic curves and vapor–liquid equilibria of the studied 2CLJQ fluids.

The second virial coefficient $B(T)$ was sampled using Monte-Carlo simulations using 200 different steps for the center of mass distance between $r_{ij,\min} = 0.2\sigma$ and $r_{ij,\max} = 20\sigma$. For each distance, 1 000 random orientations were evaluated. Ten replica MC simulations with different random seeds were

carried out for determining the second virial coefficient at a given temperature for a given fluid. The results for $B(T)$ were fitted using the empirical correlation proposed by Xu et al. [72].

For determining the characteristic curve state points by MD simulations, we follow the method proposed in Ref. [52] and used NVT simulations for determining state points for the Zeno, Boyle, and Charles curves, while NpT simulations were used for the Amagat curve. State points on the Zeno curve were identified using the condition $Z = 1$. For the Amagat curve, the condition $(\partial U/\partial V)_T = 0$ was used; for the Boyle curve the condition $(\partial Z/\partial V)_T = 0$; and for the Charles curve the condition $(\partial H/\partial p)_T = 0$. For a given fluid and characteristic curve, 9.. 11 state points were studied. From the results from such a set, one characteristic curve state point was determined [52]. The statistical uncertainties of the determined characteristic curve state points was estimated from the statistical uncertainties of the individual simulations using error propagation, cf. Ref. [52] for details. For determining a full set of thermodynamic properties at the characteristic curve state points, an additional MD simulation was carried out at each characteristic curve state point. For these simulations, the Lustig formalism [70, 73, 74] was applied, which yields the Helmholtz energy derivatives with respect to the density and the inverse temperature up to second order. Based on that data, a thermodynamic consistency test was applied for checking the corresponding conditions for the characteristic curves [52]. The MD simulations were performed using 2 000 particles in a cubic box with periodic boundary conditions. Equilibration was carried out for 100,000 time steps for NVT and an additional 100,000 time steps for NpT equilibration for subsequent NpT production simulations. The production run consisted of 750,000 time steps. A cut-off radius of 5σ was employed using the center of mass method [70]. Classical long-range corrections were applied. The time step was $\Delta\tau = 0.0005\sigma\sqrt{M/\epsilon}$. Classical velocity scaling was used for the thermostat, while Andersen's barostat was used to prescribe the pressure. The barostat piston mass was determined using the heuristic approach proposed in Ref. [52].

4 Results

The results section is structured as follows: First, the results for the zero-density limit characteristic points are presented and discussed. Then, the characteristic curve results from molecular simulation and the EOS are presented and discussed for a selection of 2CLJQ fluids (cf. grey filled symbols in Fig. 1). Then, the results for applicability of the corresponding states law for all four characteristic curves and for the linearity law for the Zeno curve are presented and discussed. Also, results for the application of a global empirical correlation of the molecular simulation results to real substances are presented. The numerical data for all molecular simulation results for all studied 2CLJQ fluids are reported in the Supplementary Material.

4.1 Zero-Density Limit Characteristic Points

Figure 2 shows the results for the zero-density limit characteristic point temperatures $T_{\text{char},i}$ as obtained from the Monte Carlo simulations. Results are shown for all 36 studied 2CLJQ fluids. The results for all $T_{\text{char},i}$ decrease with increasing L and increasing Q^2 . The Boyle temperature $T_{\text{char,Boyle}}$ of the 2CLJQ fluid was also studied by Menduiña et al. [15]. Their results are in agreement with our results.

Important differences are observed for the influence of the two molecular parameters, i.e. the elongation and the quadrupole moment. In the studied molecular parameter ranges, the characteristic point temperatures $T_{\text{char},i}$ are significantly stronger affected by the elongation compared to the quadrupole moment. Interestingly, the dipole moment was found in a recent work of our group [51] to have a significantly stronger influence on the zero-density limit characteristic point temperature compared to the quadrupole moment influence obtained here. This is in accordance with the underlying multipole expansion concept, where the point dipole represents the most significant perturbation of the unpolar molecule, whereas the point quadrupole (and higher order point multipoles) represent less significant perturbations.

4.2 Brown's Characteristic Curves

Figures 3 and 4 show the results for the characteristic curves of the 2CLJQ fluid for varying quadrupole and elongation, respectively. Figure 3 shows the results for the fluids with different quadrupole moment and constant elongation $L/\sigma = 0.505$, cf. vertically aligned grey filled symbols in Fig. 1. Figure 4 shows the results for the 2CLJQ fluids with different elongation and constant quadrupole moment $Q^2/\varepsilon\sigma^5 = 2$, cf. horizontally aligned grey filled symbols in Fig. 1. The characteristic

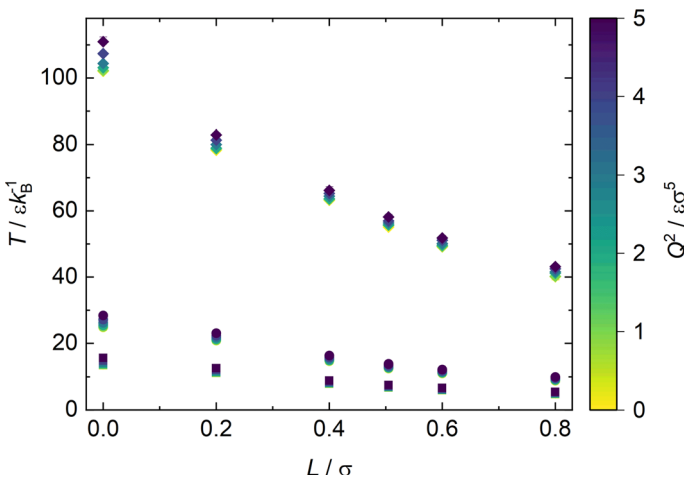


Fig. 2 Temperature of the zero-density limit characteristic points of the 2CLJQ fluids. Diamonds indicate to the zero-density limit characteristic point for the Amagat curve, bullets for the Charles curve, and the squares for the Boyle and Zeno curve. Error bars are only shown if they exceed the symbol size

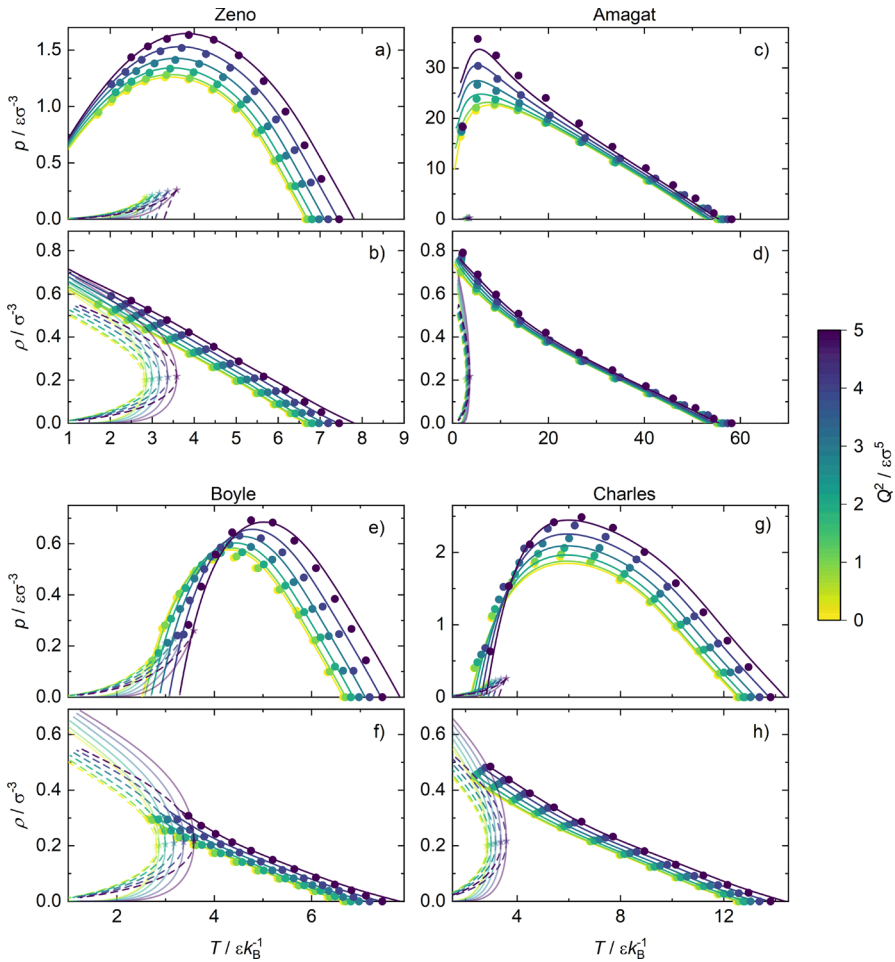


Fig. 3 Characteristic curves of 2CLJQ fluids with $L/\sigma = 0.505$ and different $Q^2/\epsilon\sigma^5$: (a) and (b) Zeno curve; (c) and (d) Amagat curve; (e) and (f) Boyle curve; (g) and (h) Charles curve. For all curves: Top plot is $p - T$ projection and bottom plot is $\rho - T$ projection. Results from the MD simulations are indicated as bullets. Statistical uncertainties lie within the symbol size. Lines indicate EOS results. The 50 % transparent lines and symbols indicate the vapor–liquid equilibrium (solid lines indicate binodal, dashed lines indicate spinodal, star indicates the critical point)

curve results are presented in the $p - T$ and the $\rho - T$ projection. The molecular simulation results are shown in comparison to the EOS results in Figs. 3 and 4.

The results from the two independent predictions (molecular simulation and EOS) are in astonishing good agreement considering the fact that the EOS model was built from two model terms that were fitted to data for moderate conditions [17, 71]. This demonstrates the capabilities of physically-based EOS models for carrying out reliable extrapolations to conditions and properties that were not considered in the model development. The influence of the quadrupole moment (at constant

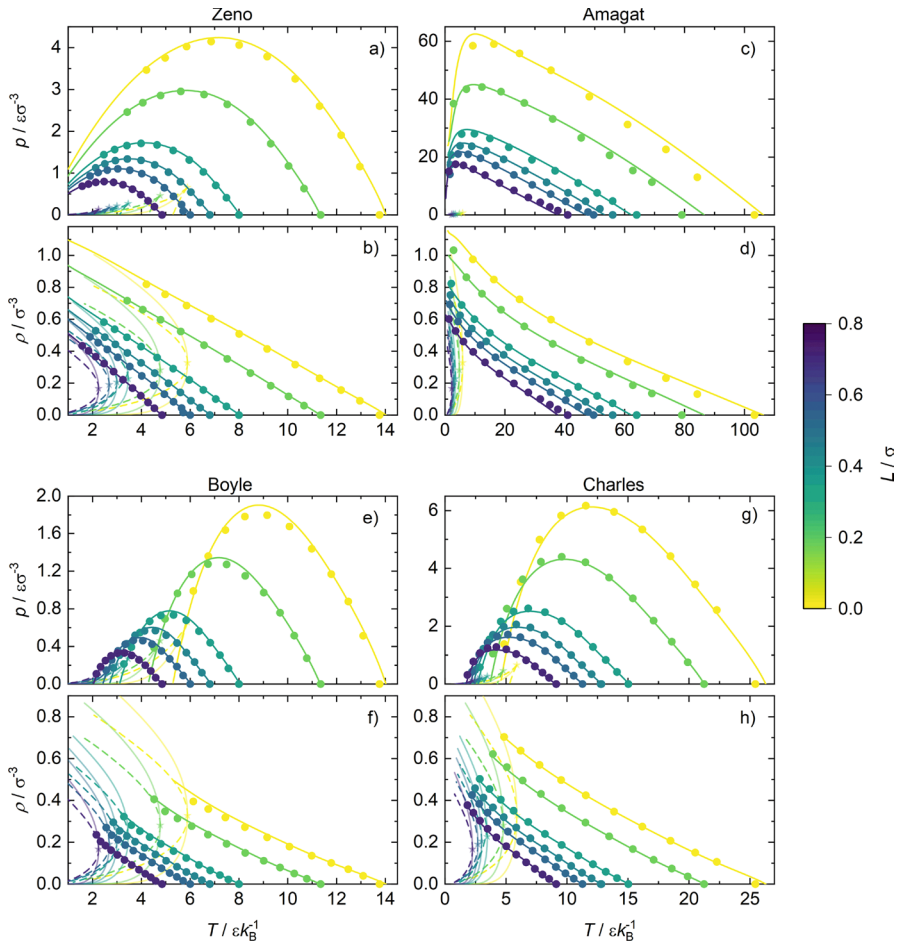


Fig. 4 Characteristic curves of 2CLJQ fluids with $Q^2/\epsilon\sigma^5 = 2$ and different L/σ : (a) and (b) Zeno curve; (c) and (d) Amagat curve; (e) and (f) Boyle curve; (g) and (h) Charles curve. For all curves: Top plot is $p - T$ projection and bottom plot is $\rho - T$ projection. Results from the MD simulations are indicated by bullets. Statistical uncertainties lie within the symbol size. Lines indicate EOS results. The 50 % transparent lines and symbols indicate the vapor–liquid equilibrium (solid lines indicate binodal, dashed lines indicate spinodal, star indicates the critical point)

elongation $L/\sigma = 0.505$) is captured very well by the Helmholtz energy model of Gross [17]. Some deviations between the molecular simulation and EOS results are observed for the zero-density limit temperatures at high quadrupole moments and in the vicinity of the vapor–liquid equilibrium, cf. Fig. 3. At the lowest temperature studied for the Amagat curve, the molecular simulation results deviate significantly from the EOS results, cf. Fig. 3c). This is due to the fact that these state points lie in the solid phase region (see Supplementary Material). The influence of the elongation (at constant $Q^2/\epsilon\sigma^5 = 2$) is essentially captured perfectly by the Helmholtz energy model of Lísal et al. [71], cf. Fig. 4. Some minor deviations are only observed for

the Amagat curve at $L = 0$ and in the vicinity of the pressure maximum of the Boyle curve. The results also indicate that the split of the Helmholtz energy terms in the ansatz (4) works very well and, accordingly, the effects of different molecular properties (interactions and architecture) can be modeled independently. The comparison to the performance of the quadrupole term (cf. Fig. 3) with the performance of the dipole term (cf. Ref. [51]) shows that the quadrupole term is significantly more accurate at extreme conditions. Since the two models are built using the same mathematical form [17, 75], the differences in the performance are possibly a result of differences in the parametrization or the applicability of the model assumptions for the first order term in the multipole expansion, i.e. the point dipole.

The influence of the molecular properties Q and L on the characteristic curves provides interesting insights. The quadrupole has only small effects on the characteristic curves (cf. Fig. 3), whereas the elongation strongly affects them (cf. Fig. 4). Moreover, the comparison of the results for the influence of the dipole moment μ (cf. Ref. [51]) with the results for the influence of the quadrupole moment Q (cf. Fig. 3) yields new insights in the effect of the different multipoles on the fluid behavior at extreme conditions: The dipole has a strong influence on the four characteristic curves, whereas the quadrupole has only a small influence. This is surprising considering the fact that the quadrupole describes a more complex electrostatic field. The fact that the quadrupole has only a relatively small effect on the fluid behavior at extreme conditions is possibly related to the symmetry of the quadrupole interaction potential caused by the $q, -2q, q$ charge distribution compared to $+q, -q$ charge distribution of the dipole.

The quality of the molecular simulation results can be assessed based on the scattering of the data, the agreement with the zero-density limit, and the Helmholtz energy consistency test. This consistency test is described in detail in Ref. [52]. The molecular simulation results show a smooth trend in practically all cases (see Figs. 3 and 4 and also Supplementary Material) and converge well to the zero-density limit temperatures. The results for the Helmholtz energy consistency test are presented in Fig. 5. The Helmholtz energy criteria for the characteristic curves is fulfilled by 54 % of the data points for the Zeno curve, 61 % for the Amagat curve, 67 % for the Boyle curve, and 59 % for the Charles curve. These values are slightly better compared to the results for the 2CLJD study, cf. Ref. [51]. This is probably due to the fact that the EOS for the 2CLJQ fluid yields better initial guess values compared to the EOS used in the 2CLJD study. Overall, the molecular simulation results for the studied 2CLJQ fluid are reasonably well conform with the Helmholtz energy test, cf. Fig. 5. Yet, some systematic deviations are observed in the case of the Charles curve, cf. Fig. 5. At low temperatures, the Helmholtz energy test indicates that the obtained characteristic curve state points slightly overestimate the true values. These deviations are possible due to the fact that the simulations were carried out in the direct vicinity of the vapor–liquid equilibrium binodal. Furthermore, at low temperatures, some data points show large deviations from the Helmholtz energy criterion for the Amagat curve. For most of these state points, crystallization occurred in the simulations (cf. Supplementary Material).

Figure 6 shows the results for the 2CLJQ fluid with $L/\sigma = 0.505$ and $Q^2/\epsilon\sigma^5 = 2$ in the double logarithmic p, T -diagram. The results are fully conform with *Brown's*

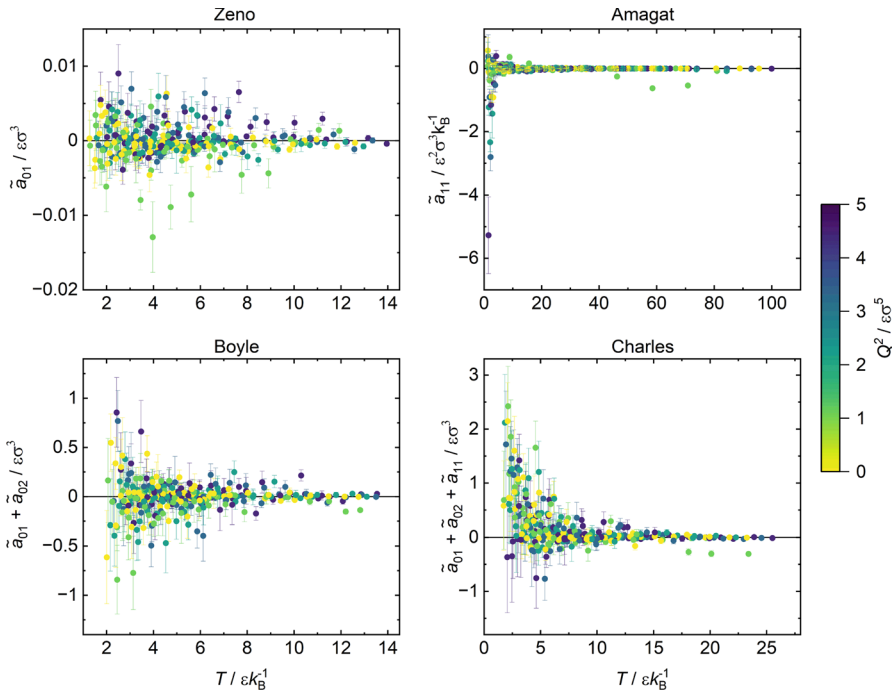


Fig. 5 Results of thermodynamic consistency test of the Helmholtz energy criteria. Molecular simulation results for all 36 studied 2CLJQ fluids

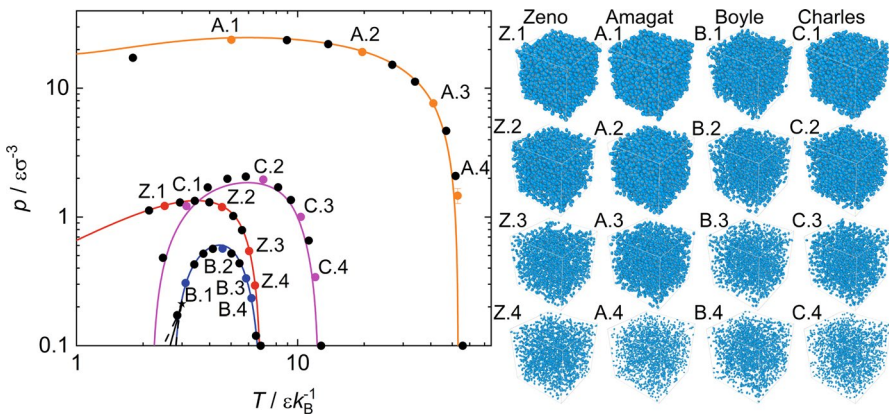


Fig. 6 Visualization of the MD simulations for the characteristic curves for the 2CLJQ fluid with $L/\sigma = 0.505$ and $Q^2/\epsilon\sigma^5 = 2$. Left side: Lines indicate EOS results (Zeno: red, Amagat: orange, Boyle: blue, and Charles: pink). Bullets indicate characteristic curve state points obtained from molecular simulation. For the colored bullets, the visualization of the atomistic configuration is shown (right side). In the visualization, Lennard–Jones sites are represented as blue spheres; the quadrupole is indicated as grey sphere. The visualization is presented for the time step 750,000 of the production run (Color figure online)

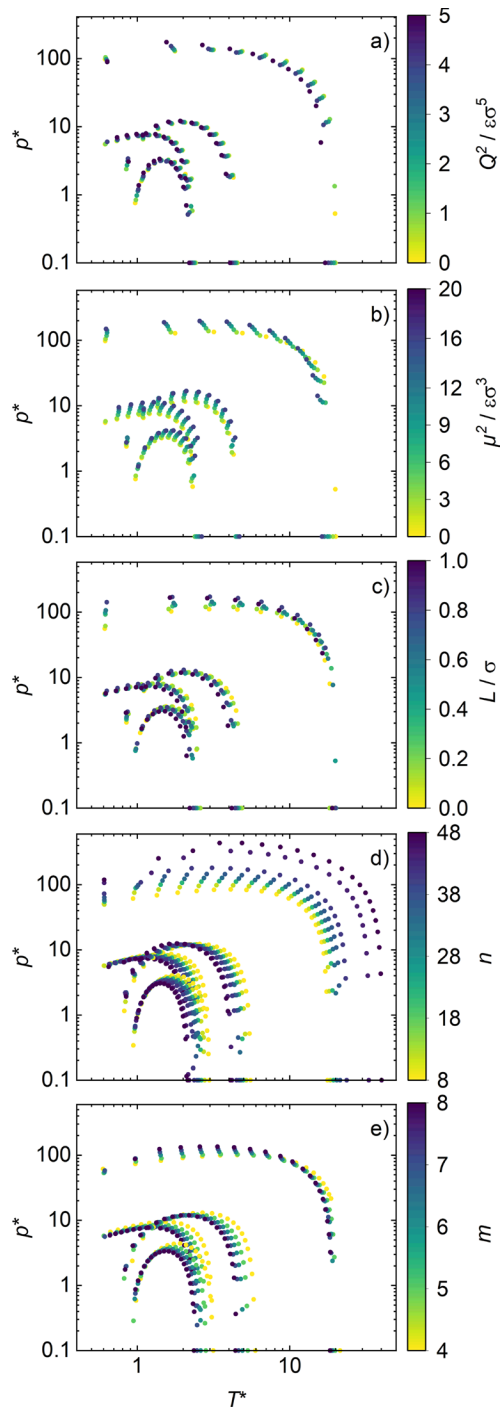
postulates regarding the topology of the characteristic curves. This also holds for all other studied 2CLJQ fluids (see Supplementary Material). This is interesting considering the fact Brown originally considered simple fluids (spherical with only dispersive and repulsive interactions). The findings for the 2CLJQ fluids are in line with what was found for dipolar fluids [51]. Additionally, for selected state points, simulation screenshots obtained from the production phase of the final simulations at the characteristic curve state points are given. This illustrates the structure of the fluid phases and the change along a characteristic curve. Starting in the zero-density limit, the Monte Carlo simulation results indicate structures with two molecules, i.e. dimers. Moving along the characteristic curves, the density increases and a given particle interacts with multiple neighboring particles, cf. Fig. 6.

4.3 Corresponding States Principle

The principle of corresponding states formulates that substances share identical reduced states with respect to their critical properties [57, 58]. The corresponding states principle is frequently applied to model fluid properties [76–78]. The corresponding states principle was originally derived for simple fluids, i.e. spherical molecules with repulsive and dispersive interactions such as argon. It is, accordingly, often used to study the perturbation effect of complex interaction features on the corresponding states principle. Hence, it is used to quantify the deviations from the 'ideal fluid behavior' caused by different molecular architectures and interactions. The applicability of the corresponding states principle has been extensively studied in the literature for different molecular properties such as the Mie potential parameters [29, 65, 79, 80], the cut-off distances [81, 82], the shape and elongation of the molecules [83–87], and mixtures [39, 88–90]. The deviations from the corresponding states law caused by these molecular properties were for example studied for virial coefficients [15, 86], vapor–liquid equilibrium properties [89, 91–93], and interfacial properties [39, 65, 82]. However, the influence of quadrupolar interactions on deviations from an 'ideal fluid behavior' characterized by the corresponding states principle for homogeneous state properties at extreme conditions have not been investigated yet. For fluids that follow the corresponding states law, results for a given characteristic curve should collapse to a common master curve if plotted in reduced units with respect to the critical parameters.

We have applied the corresponding states principle to the molecular simulation results for the 2CLJQ characteristic curve results. For the critical point of the 2CLJQ fluids, the empirical correlation from Stoll et al. [11] was used. Figure 7 shows the results obtained for all studied 2CLJQ fluids in comparison to results from other model fluid classes. Thereby, the deviations from the ideal corresponding states principle caused by quadrupole interactions (cf. Fig. 7a) are compared to those caused by dipole interactions (cf. Fig. 7b), the elongation of the molecule (cf. Fig. 7c), and the shape of the Mie potential, i.e. the repulsive exponent (cf. Fig. 7d) and the attractive exponent (cf. Fig. 7e). The data for the 2CLJD and Mie fluids were taken from Refs. [29, 51]. For all shown model fluid classes, the Lennard–Jones fluid can be considered the 'ideal' reference fluid.

Fig. 7 Characteristic curves in terms of reduced units with respect to the corresponding critical parameters in the double-logarithmic pressure-temperature projection for: (a) 2CLJQ fluids, (b) 2CLJD fluids, (c) 2CLJ fluids, (d) Mie $n,6$ fluids, and (e) Mie $12,m$ fluids. The data for the 2CLJD and Mie fluids are taken from Refs. [29, 51]. The color code represents the different variable for each fluid class (Color figure online)



The characteristic curves of the 2CLJQ fluids with different quadrupole moment (at constant L) satisfy the principle of corresponding states very well (cf. Fig. 7a). For the fluids with different dipole moment (cf. Fig. 7b), on the other hand, significant deviations from the corresponding states principle are observed—especially for the Zeno, Boyle, and Charles curve. These differences for the quadrupolar and dipolar fluids are in line with the observations discussed above for the absolute influence of Q and μ on the characteristic curves and is probably related to the stronger symmetry of the quadrupole potential compared to dipole potential. Interestingly, the quadrupole moment Q of the 2CLJQ fluids and the elongation L of 2CLJ fluids are found to cause an overall similar deviation of the corresponding states law, cf. Fig. 7a and c.

Similarly, also the attractive Mie interaction parameter m causes only moderate deviations from the corresponding states law (cf. Fig. 7e). Surprisingly, the repulsive Mie exponent n is found to cause significant deviations from the corresponding states law (cf. Fig. 7d)—especially compared to the polar interactions (cf. Fig. 7a, b). This is interesting considering the fact that 2CLJQ and 2CLJD fluids exhibit evidently important deviations from a spherical molecule, which is a central argument in the corresponding states principle. Hence, for the 2CLJQ and 2CLJD fluids, mean field effects of the interactions probably compensate the anisotropy of the interaction potential.

Table 1 presents the results for the characteristic points in reduced units for a subset of 2CLJQ fluids. The results for the reduced temperature $T^* = T/T_c$ and reduced pressure $p^* = p/p_c$ of the pressure maxima for the different curves are reported. The

Table 1 Pressure maximum p_{\max} and zero-density limit characteristic points for the characteristic curves of the 2CLJQ fluids

L/σ	$Q^2/\epsilon\sigma^5$	Zeno			Amagat			Boyle			Charles		
		p_{\max}		$\lim_{\rho \rightarrow 0}$	p_{\max}		$\lim_{\rho \rightarrow 0}$	p_{\max}		$\lim_{\rho \rightarrow 0}$	p_{\max}		$\lim_{\rho \rightarrow 0}$
		T^*	p^*	T^*_{char}	T^*	p^*	T^*_{char}	T^*	p^*	T^*_{char}	T^*	p^*	T^*_{char}
0	2	1.25	8.00	2.46	2.45	114.25	18.50	1.57	3.49	2.46	2.11	11.90	4.55
0.2	2	1.26	7.58	2.50	2.33	113.63	17.40	1.56	3.31	2.50	2.09	11.28	4.67
0.4	2	1.23	7.70	2.42	2.22	128.75	19.33	1.54	3.33	2.42	2.04	11.78	4.54
0.6	2	1.19	7.59	2.33	2.20	148.76	19.26	1.49	3.22	2.33	1.97	11.78	4.38
0.8	2	1.16	7.82	2.25	1.96	173.13	19.00	1.47	3.27	2.25	1.88	12.55	4.23
0.505	0	1.24	7.50	2.41	2.88	134.36	20.00	1.54	3.26	2.41	2.08	11.54	4.54
0.505	1	1.22	7.52	2.40	2.72	134.71	19.87	1.53	3.27	2.40	2.05	11.61	4.52
0.505	2	1.21	7.56	2.36	2.26	137.80	19.44	1.52	3.24	2.36	1.99	11.66	4.43
0.505	3	1.19	7.52	2.31	2.05	143.81	18.69	1.47	3.20	2.31	1.94	11.68	4.32
0.505	4	1.14	7.58	2.25	1.90	153.13	17.94	1.46	3.17	2.25	1.85	11.88	4.19
0.505	5	1.15	7.94	2.19	1.79	176.26	17.12	1.45	3.38	2.19	1.85	12.10	4.07

A subset of studied fluids with different elongation L/σ and quadrupole moment $Q^2/\epsilon\sigma^5 = 2$ and fluids $L/\sigma = 0.505$ with different quadrupole moment is shown (results for the other fluids are presented in the Supplementary Material). Results are presented as reduced temperature $T^* = T/T_c$ and $p^* = p/p_c$. Critical point properties were computed from the correlation of Stoll et al. [11]

values are obtained by using spline interpolation of the simulation data in the vicinity of the respective point. The results for the reduced zero-density limit characteristic point T_{char}^* are presented as well. The numeric results support the qualitative findings from Fig. 7, i.e. the different 2CLJQ fluids follow the corresponding states law well.

4.4 Linearity Law

The linearity law for the Zeno curve, first described by Batschinski in 1906 [53], postulates that the Zeno curve in the $\rho - T$ projection follows a straight line. We tested *Batschinski's* linearity law for the 2CLJQ fluids studied in this work. Therefore, a linear fit was computed for the Zeno curve molecular simulation data for each 2CLJQ fluid. For this fit, the zero-density limit, i.e. Boyle temperature, obtained from the MC simulations was prescribed as fix-point. The results for the 2CLJQ fluid with $L/\sigma = 0.505$ and $Q^2/\varepsilon\sigma^5 = 2$ are exemplarily shown in Fig. 8. For comparison, also the independent predictions from the EOS are shown. The molecular simulation Zeno curve results follow the linearity law reasonably well, but deviations are observed between the MD simulations and the linear fit. Notably, these deviations exceed the uncertainties of the simulation results. The simulation results show a faint concave curvature in the entire temperature range.

Figure 9 shows the deviation plot for all investigated 2CLJQ fluids in reduced units in terms of $T^* = T/T_c$ and $\rho_{\text{res}}^* = \rho_{\text{res}}/\rho_c$, where T_c and ρ_c indicate the critical values of a given fluid. Critical point values were computed from the correlation of Ref. [11]. The deviations from *Batschinski's* linearity law are qualitatively similar for all studied 2CLJQ fluids, cf. Figure 9. In all cases, the deviations exceed the statistical uncertainties of the molecular simulation results. The deviations increase with increasing elongation L . The quadrupole moment has only a minor influence on the deviations from the linearity law (see Supplementary Material for details). Only

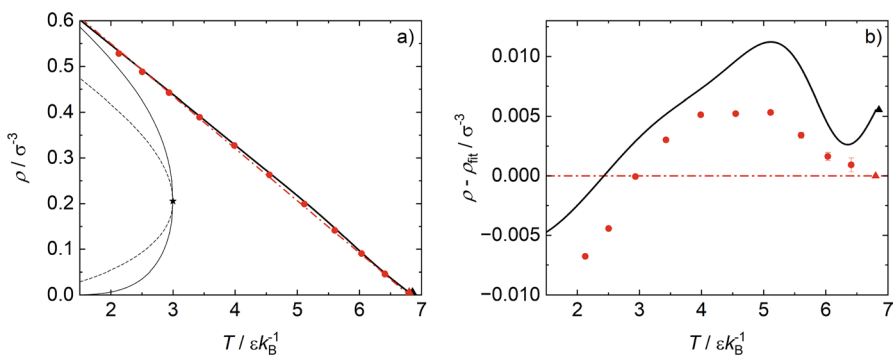


Fig. 8 Test of the linearity-law for the Zeno curve for the 2CLJQ fluid with $L/\sigma = 0.505$ and $Q^2/\varepsilon\sigma^5 = 2$. (a) Results in the $\rho - T$ projection; (b) deviation plot with the linear fit as baseline. Red bullets indicate MD simulation results; red triangle the MC Boyle temperature result. Red dashed line indicates the linear fit for the MD simulation results. Black lines and symbols indicate EOS results: binodal: thin solid line; spinodal: thin dashed line; Zeno curve: solid line; critical point: star; Boyle temperature: triangle. Error bars are only shown if they exceed the symbol size

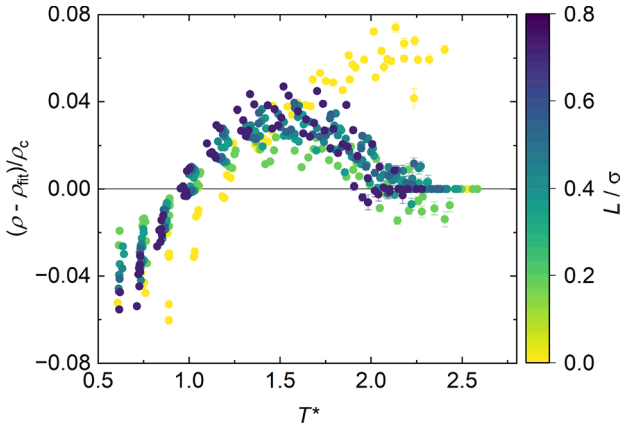


Fig. 9 Deviation plot for the assessment of the linearity law for the Zeno curve in terms of reduced residual density ρ_{res}^* and reduced temperature T^* . Results are presented for all 36 studied 2CLJQ fluids

for the fluids with $L = 0$, the MD results show a special behavior as they yield the largest deviations and do not converge as smoothly to the Boyle temperature values.

To quantify the deviations from *Batschinski's* linearity law, the absolute average deviation (AAD) between the linear fit and the molecular simulation results was calculated as

$$\text{AAD} = \frac{1}{N} \sum_{i=1}^N \left| \frac{\rho_i^{\text{MD}} - \rho_i^{\text{fit}}}{\rho_i^{\text{MD}}} \right| \cdot 100\%, \quad (5)$$

where N indicates the number of characteristic curve state points obtained from MD simulations. For the 2CLJQ fluids, the AAD value is calculated to be 1.2 %. We have compared the applicability of the linearity law for the 2CLJD and 2CLJQ fluid class. The results are presented in the Supplementary Material. The 2CLJQ fluid results are in better agreement with the linearity law than the 2CLJD fluids. For the latter, we obtained an $\text{AAD} = 2.2\%$, cf. Eq. 5. Hence, the deviations from the 'ideal' Zeno curve behavior are for dipole interactions almost twice as large as for quadrupolar interactions. This is in line with the findings for the corresponding states law, cf. Fig. 7.

4.5 Application of 2CLJQ Characteristic Curve Model to Real Substances

Global empirical correlations were developed for describing the characteristic curves of the 2CLJQ fluid class and applied to real substances. They are formulated for each characteristic curve individually as the reduced pressure $p^* = p/p_c$ as a function of the reduced temperature $T^* = T/T_c$ as well as the model parameters Q and L . The mathematical form and the parameters are given in the Supplementary Material. The parameters of the empirical model were fitted to the molecular simulation data.

Table 2 Substance model parameters of carbon dioxide (CO₂), R116 (C₂F₆), and R1270 (C₃H₆)

	$\sigma/\text{\AA}$	$\varepsilon/k_{\text{B}}\text{K}^{-1}$	$L/\text{\AA}$	$Q/D\text{\AA}$	L/σ	$Q^2/\varepsilon\sigma^5$	References
CO ₂	2.9847	133.22	2.4176	3.7938	0.80999	3.30364	[4]
R116	4.1282	110.19	2.7246	8.4943	0.65999	3.95572	[4]
R1270	3.8169	150.78	2.5014	5.9387	0.65535	2.09123	[4]

Model parameters in SI units and reduced model parameters L/σ and $Q^2/\varepsilon\sigma^5$ in the reduced LJ unit system used for evaluating the characteristic curve correlations

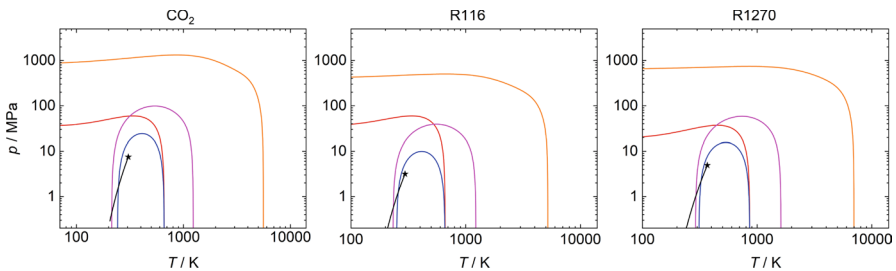


Fig. 10 Characteristic curves in the $p - T$ projection of CO₂ (left), R116 (middle), and R1270 (right). Results from the empirical correlation evaluated for the molecular models given in Table 2. Results for the Zeno (red), Amagat (orange), Boyle (blue), and Charles (pink) curve. Binodal (black) and critical point (star) were computed from the empirical correlation from Ref. [11] (Color figure online)

The empirical model was applied for modeling the characteristic curves of real substances. Three real substances were considered, namely: carbon dioxide (CO₂) and the refrigerants R116 (C₂F₆) and R1270 (C₃H₆). The model parameters were taken from the MolMod database [9]. The models were developed by Vrabec et al. [4]. The model parameters are given in Table 2. The elongation parameter value for the R116 and R1270 model are very similar—only the quadrupole moment differs by a factor of approximately two, cf. Table 2.

The results are shown in Fig. 10. The vapor–liquid equilibrium binodal depicted in Fig. 10 was computed using the empirical correlation proposed by Stoll et al. [11]. For all three investigated substances, the characteristic curves are conform with the expected behavior in the fluid region. At very low temperatures (where solidification occurs), the empirical models are not valid and yield unrealistic results. Especially for refrigerants and classical gases, the empirical correlation can be straightforwardly used for estimating for example the Charles curve (which corresponds to the Joule–Thomson inversion).

5 Conclusion

We carried out a systematic study of *Brown's* characteristic curves for the 2CLJQ model class. This provides new insights in the influence of quadrupole interactions on the fluid behavior at extreme temperature and pressure conditions. The

quadrupole interactions have a surprisingly small influence on the macroscopic property fluid behavior described by the characteristic curves. The point quadrupole describes a relatively complex charge distribution and yields a significant anisotropy of the overall interaction potential. Yet, the Zeno, Amagat, Boyle, and Charles curve show only a moderate sensitivity to quadrupole interactions. Moreover, it is interesting to note that the lower-order and less complex charge distribution, i.e. the point dipole has a significantly stronger influence on the characteristic curves compared to the point quadrupole. Especially for the Amagat curve, the quadrupole is found to have only a minor influence. For future work, it would be interesting to study the different effects of dipole and quadrupole interactions at extreme conditions also for other characteristic properties such as the self-diffusion coefficient and distribution functions.

The differences for the dipole and quadrupole interactions are supported by the results for the corresponding states law and *Batschinski's* linearity law. The deviations of the fluid behavior from these laws can be taken as a measure for the non-ideality of the molecular interactions, where ideal means spherical particles with simple repulsive and dispersive interactions. For the corresponding states law, point dipole interactions yield stronger deviations from the ideal behavior compared to quadrupole interactions. Similar findings are obtained for *Batschinski's* linearity law, i.e. point dipole interactions yield a stronger deviation from the ideal behavior compared to quadrupole interactions.

Interesting insights are obtained from the comparison of different model fluid classes regarding their characteristic curves. By comparing results for the 2CLJQ, 2CLJD, and Mie fluid class, we elucidated the relation of different of molecular features on the fluid behavior at extreme conditions. Surprisingly, the polar interactions cause only minor perturbations of the 'ideal' fluid behavior described by the corresponding states principle and a simple reference fluid. Similarly, the molecule elongation of the 2CLJ model class as well as the attractive Mie potential parameter have only a minor influence on the fluid behavior expressed by the characteristic curves. The Mie potential repulsive parameter, on the other hand, is found to cause important perturbations of the 'ideal' fluid behavior.

Moreover, the comparison of the predictions from the molecular-based EOS and the first principle molecular simulation results for the case of the 2CLJQ and 2CLJD fluids yields novel insights in the extrapolation capabilities of the EOS model terms: The 2CLJ model of Lísal et al. [71] yields an excellent description over a wide elongation parameter range for all four characteristic curves. Also the quadrupole term proposed by Gross [17] shows an excellent performance. The dipole term of Gross and Vrabec [75], on the other hand, yields some deviations to the computer experiment reference data. Since both, the dipole and the quadrupole term, are built using a similar mathematical form, the differences in the performance are likely either due to the respective parametrization and/or problems regarding the applicability of the model assumptions in the dipole term. Nevertheless, all molecular-based EOS models yield qualitatively accurate results and in some cases—especially the 2CLJQ case—astonishing quantitative accuracy. This is attributed to the strong physical backbone of the models that provide

an excellent extrapolation behavior well beyond the property and thermodynamic condition range considered for the model development.

Furthermore, we have established an empirical correlation of the computer experiment data as a global function of the model parameters for the 2CLJQ fluid characteristic curves using critical point data obtained by the correlation from Stoll et al. [11] and the zero-density limit values. This provides a practical tool for estimating the characteristic curves—especially the Joule–Thomson inversion—for real substance fluids.

Polar interactions are important for many real substances. The 2CLJD and 2CLJQ model classes provide valuable tools for investigating the role and effects of polar interactions for macroscopic properties. Also, these model classes establish a direct link to real substance models that are relevant for many technical applications. The behavior of polar interactions at extreme conditions studied in this work yields some surprising insights, e.g. in the differences observed for the dipole and quadrupole interactions. These effects are not yet fully understood on the atomistic level and require further investigations.

Supplementary Information The online version contains supplementary material available at <https://doi.org/10.1007/s10765-024-03367-7>.

Acknowledgements The simulations were carried out on the HPC machine ELWE at the RHRZ under the grant RPTU-MTD and on the HPC machine MOGON at the NHR SW under the grant TU-MSG (supported by the Federal Ministry of Education and Research and the state governments).

Author Contributions H. Renneis: Data curation, formal analysis, visualisation, and writing/original draft preparation (support); S. Stephan: conceptualization, methodology, supervision, writing/original draft preparation (lead), and funding acquisition.

Funding Open Access funding enabled and organized by Projekt DEAL. We gratefully acknowledge funding from the European Union's Horizon Europe research and innovation programme under grant Agreement No. 101137725 (BatCAT).

Data Availability Data is provided within the manuscript or supplementary information files.

Declarations

Conflict of interest The authors have no conflict of interest to declare.

Open Access This article is licensed under a Creative Commons Attribution 4.0 International License, which permits use, sharing, adaptation, distribution and reproduction in any medium or format, as long as you give appropriate credit to the original author(s) and the source, provide a link to the Creative Commons licence, and indicate if changes were made. The images or other third party material in this article are included in the article's Creative Commons licence, unless indicated otherwise in a credit line to the material. If material is not included in the article's Creative Commons licence and your intended use is not permitted by statutory regulation or exceeds the permitted use, you will need to obtain permission directly from the copyright holder. To view a copy of this licence, visit <http://creativecommons.org/licenses/by/4.0/>.

References

1. C.G. Gray, K.E. Gubbins, *Theory of Molecular Fluids*, vol. 1 (Fundamentals. Clarendon Press, Oxford, 1984)
2. J. Tomasi, B. Mennucci, R. Cammi, Quantum mechanical continuum solvation models. *Chem. Rev.* **105**, 2999–3094 (2005). <https://doi.org/10.1021/cr9904009>
3. J. Stoll, J. Vrabec, H. Hasse, A set of molecular models for carbon monoxide and halogenated hydrocarbons. *J. Chem. Phys.* **119**, 11396–11407 (2003). <https://doi.org/10.1063/1.1623475>
4. J. Vrabec, J. Stoll, H. Hasse, A set of molecular models for symmetric quadrupolar fluids. *J. Phys. Chem. B* **105**, 12126–12133 (2001). <https://doi.org/10.1021/jp012542o>
5. J.-P. Bouanich, Site-site Lennard–Jones potential parameters for N₂, O₂, H₂, CO and CO₂. *J. Quant. Spectrosc. Radiat. Transf.* **47**, 243–250 (1992). [https://doi.org/10.1016/0022-4073\(92\)90142-Q](https://doi.org/10.1016/0022-4073(92)90142-Q)
6. D. Möller, J. Fischer, Determination of an effective intermolecular potential for carbon dioxide using vapour-liquid phase equilibria from NpT + test particle simulations. *Fluid Phase Equilib.* **100**, 35–61 (1994). [https://doi.org/10.1016/0378-3812\(94\)80002-2](https://doi.org/10.1016/0378-3812(94)80002-2)
7. K. Stöbener, P. Klein, M. Horsch, K. Küfer, H. Hasse, Parametrization of two-center Lennard–Jones plus point-quadrupole force field models by multicriteria optimization. *Fluid Phase Equilib.* **411**, 33–42 (2016). <https://doi.org/10.1016/j.fluid.2015.11.028>
8. L. Meng, Y.-Y. Duan, Site-site potential function and second virial coefficients for linear molecules. *Mol. Phys.* **104**, 2891–2899 (2006). <https://doi.org/10.1080/00268970600867338>
9. S. Stephan, M. Horsch, J. Vrabec, H. Hasse, MolMod - an open access database of force fields for molecular simulations of fluids. *Mol. Simul.* **45**, 806–814 (2019). <https://doi.org/10.1080/08927022.2019.1601191>
10. S. Schmitt, G. Kanagalingam, F. Fleckenstein, D. Froescher, H. Hasse, S. Stephan, Extension of the MolMod database to transferable force fields. *J. Chem. Inf. Model.* **63**, 7148–7158 (2023). <https://doi.org/10.1021/acs.jcim.3c01484>
11. J. Stoll, J. Vrabec, H. Hasse, J. Fischer, Comprehensive study of the vapour-liquid equilibria of the pure two-centre Lennard–Jones plus pointquadrupole fluid. *Fluid Phase Equilib.* **179**, 339–362 (2001). [https://doi.org/10.1016/s0378-3812\(00\)00506-9](https://doi.org/10.1016/s0378-3812(00)00506-9)
12. S. Werth, M. Horsch, H. Hasse, Surface tension of the two center Lennard–Jones plus quadrupole model fluid. *Fluid Phase Equilib.* **392**, 12–18 (2015). <https://doi.org/10.1016/j.fluid.2015.02.003>
13. S. Werth, K. Stöbener, P. Klein, K.-H. Küfer, M. Horsch, H. Hasse, Molecular modelling and simulation of the surface tension of real quadrupolar fluids. *Chem. Eng. Sci.* **121**, 110–117 (2015). <https://doi.org/10.1016/j.ces.2014.08.035>
14. S. Homes, M. Heinen, J. Vrabec, Influence of molecular anisotropy and quadrupolar moment on evaporation. *Phys. Fluids* **35**, 052111 (2023). <https://doi.org/10.1063/5.0147306>
15. C. Mendiña, C. McBride, C. Vega, The second virial coefficient of quadrupolar two center Lennard–Jones models. *Phys. Chem. Chem. Phys.* **3**, 1289–1296 (2001). <https://doi.org/10.1039/B009509P>
16. L.G. MacDowell, C. Mendiña, C. Vega, E. Miguel, Third virial coefficients and critical properties of quadrupolar two center Lennard–Jones models. *Phys. Chem. Chem. Phys.* **5**, 2851–2857 (2003). <https://doi.org/10.1039/b302780e>
17. J. Gross, An equation-of-state contribution for polar components: quadrupolar molecules. *AIChE J.* **51**, 2556–2568 (2005). <https://doi.org/10.1002/aic.10502>
18. B. Saager, J. Fischer, Construction and application of physically based equations of state: Part II. The dipolar and quadrupolar contributions to the Helmholtz energy. *Fluid Phase Equilib.* **72**, 67–88 (1992). [https://doi.org/10.1016/0378-3812\(92\)85019-5](https://doi.org/10.1016/0378-3812(92)85019-5)
19. K.E. Gubbins, Perturbation theories of the thermodynamics of polar and associating liquids: A historical perspective. *Fluid Phase Equilib.* **416**, 3–17 (2016). <https://doi.org/10.1016/j.fluid.2015.12.043>
20. A. Szeri, Hydrodynamic and elasto-hydrodynamic lubrication, in *Modern Tribology Handbook, vol. 1: Principles of Tribology*, 1st edn. (CRC Press, Boca Raton, 2000)
21. P. Wingertszahn, S. Schmitt, S. Thielen, M. Oehler, B. Magyar, O. Koch, H. Hasse, S. Stephan, Measurement, modelling, and application of lubricant properties at extreme pressures. *Tribol. Schmierungstech.* **70**, 5–12 (2023). <https://doi.org/10.24053/tus-2023-0017>

22. S. Stephan, S. Schmitt, H. Hasse, H.M. Urbassek, Molecular dynamics simulation of the Stribeck curve: Boundary lubrication, mixed lubrication, and hydrodynamic lubrication on the atomistic level. *Friction* **11**, 2342–2366 (2023). <https://doi.org/10.1007/s40544-023-0745-y>
23. T. Mikal-Evans, D.K. Sing, J.K. Barstow, T. Kataria, J. Goyal, N. Lewis, J. Taylor, N.J. Mayne, T. Daylan, H.R. Wakeford, M.S. Marley, J.J. Spake, Diurnal variations in the stratosphere of the ultrahot giant exoplanet WASP-121b. *Nat. Astron.* **6**, 471–479 (2022). <https://doi.org/10.1038/s41550-021-01592-w>
24. R. Orosei, S.E. Lauro, E. Pettinelli, A. Cicchetti, M. Coradini, B. Cosciotti, F. Di Paolo, E. Flamini, E. Mattei, M. Pajola, F. Soldovieri, M. Cartacci, F. Cassenti, A. Frigeri, S. Giuppi, R. Martufi, A. Masdea, G. Mitri, C. Nenna, R. Noschese, M. Restano, R. Seu, Radar evidence of subglacial liquid water on Mars. *Science* **361**, 490–493 (2018). <https://doi.org/10.1126/science.aar7268>
25. F. Schipperski, A. Liebscher, M. Gottschalk, G. Franz, Re-examination of the heterotype solid solution between calcite and strontianite and Ca–Sr fluid-carbonate distribution: An experimental study of the $\text{CaCO}_3\text{--SrCO}_3\text{--H}_2\text{O}$ system at 0.5–5 kbar and 600 °C. *Am. Miner.* **106**, 1016–1025 (2021). <https://doi.org/10.2138/am-2021-7783>
26. V. Rozsa, D. Pan, F. Giberti, G. Galli, Ab initio spectroscopy and ionic conductivity of water under earth mantle conditions. *Proc. Natl Acad. Sci. U.S.A.* **115**, 6952–6957 (2018). <https://doi.org/10.1073/pnas.1800123115>
27. E.H. Brown, On the thermodynamic properties of fluids. *Bull. Inst. Int. Froid* **1960–1961**, 169–178 (1960)
28. U.K. Deiters, A. Neumaier, Computer simulation of the characteristic curves of pure fluids. *J. Chem. Eng. Data* **61**, 2720–2728 (2016). <https://doi.org/10.1021/acs.jced.6b00133>
29. S. Stephan, M. Urschel, Characteristic curves of the Mie fluid. *J. Mol. Liq.* **383**, 122088 (2023). <https://doi.org/10.1016/j.molliq.2023.122088>
30. O.L. Boshkova, U.K. Deiters, Soft repulsion and the behavior of equations of state at high pressures. *Int. J. Thermophys.* **31**, 227–252 (2010). <https://doi.org/10.1007/s10765-010-0727-7>
31. U.K. Deiters, K.M. De Reuck, Guidelines for publication of equations of state—I. Pure fluids. *Chem. Eng. J.* **69**, 69–81 (1998). [https://doi.org/10.1016/S1385-8947\(97\)00070-3](https://doi.org/10.1016/S1385-8947(97)00070-3)
32. M. Thol, G. Rutkai, R. Span, J. Vrabec, R. Lustig, Equation of state for the Lennard–Jones truncated and shifted model fluid. *Int. J. Thermophys.* **36**, 25 (2015). <https://doi.org/10.1007/s10765-014-1764-4>
33. R. Span, W. Wagner, On the extrapolation behavior of empirical equations of state. *Int. J. Thermophys.* **18**, 1415–1443 (1997). <https://doi.org/10.1007/BF02575343>
34. M. Thol, G. Rutkai, A. Koester, M. Kortmann, R. Span, J. Vrabec, Fundamental equation of state for ethylene oxide based on a hybrid dataset. *Chem. Eng. Sci.* **121**, 87–99 (2015). <https://doi.org/10.1016/j.ces.2014.07.051>
35. G. Chaparro, E.A. Müller, Development of thermodynamically consistent machine-learning equations of state: application to the Mie fluid. *J. Chem. Phys.* (2023). <https://doi.org/10.1063/5.0146634>
36. W. Wagner, A. Pruß, The IAPWS formulation 1995 for the thermodynamic properties of ordinary water substance for general and scientific use. *J. Phys. Chem. Ref. Data* **31**, 387–535 (2002). <https://doi.org/10.1063/1.1461829>
37. R. Span, W. Wagner, Equations of state for technical applications. I. Simultaneously optimized functional forms for nonpolar and polar fluids. *Int. J. Thermophys.* **24**, 1–39 (2003). <https://doi.org/10.1023/A:1022390430888>
38. J. Staubach, S. Stephan, Prediction of thermodynamic properties of fluids at extreme conditions: Assessment of the consistency of molecular-based models, in *Proceedings of the 3rd Conference on Physical Modeling for Virtual Manufacturing Systems and Processes*, ed. by J.C. Aurich, C. Garth, B.S. Linke (Springer, Cham, 2023), pp. 170–188
39. S. Stephan, U.K. Deiters, Characteristic curves of the Lennard–Jones fluid. *Int. J. Thermophys.* **41**, 147 (2020). <https://doi.org/10.1007/s10765-020-02721-9>
40. A. Neumaier, U.K. Deiters, The characteristic curves of water. *Int. J. Thermophys.* **37**, 96 (2016). <https://doi.org/10.1007/s10765-016-2098-1>
41. A. Pakraves, H. Zarei, Prediction of Joule–Thomson coefficients and inversion curves of natural gas by various equations of state. *Cryogenics* **118**, 103350 (2021). <https://doi.org/10.1016/j.cryogenics.2021.103350>
42. E.M. Apfelbaum, V.S. Vorob'ev, The similarity law for the Joule–Thomson inversion line. *J. Phys. Chem. B* **118**, 12239–12242 (2014). <https://doi.org/10.1021/jp506726v>

43. F. Castro-Marcano, C.G. Olivera-Fuentes, C.M. Colina, Joule–Thomson inversion curves and third virial coefficients for pure fluids from molecular-based models. *Ind. Eng. Chem. Res.* **47**, 8894–8905 (2008). <https://doi.org/10.1021/ie800651q>
44. A. Chacin, J.M. Vazquez, E.A. Mueller, Molecular simulation of the Joule–Thomson inversion curve of carbon dioxide. *Fluid Phase Equilib.* **165**, 147–155 (1999). [https://doi.org/10.1016/S0378-3812\(99\)00264-2](https://doi.org/10.1016/S0378-3812(99)00264-2)
45. C.M. Colina, E.A. Müller, Molecular simulation of Joule–Thomson inversion curves. *Int. J. Thermophys.* **20**, 229–235 (1999). <https://doi.org/10.1023/A:1021402902877>
46. C.M. Colina, M. Lísal, F.R. Siperstein, K.E. Gubbins, Accurate CO₂ Joule–Thomson inversion curve by molecular simulations. *Fluid Phase Equilib.* **202**, 253–262 (2002). [https://doi.org/10.1016/S0378-3812\(02\)00126-7](https://doi.org/10.1016/S0378-3812(02)00126-7)
47. S. Figueroa-Gerstenmaier, M. Lísal, I. Nezbeda, W.R. Smith, V.M. Trejos, Prediction of isoenthalps, Joule–Thomson coefficients and Joule–Thomson inversion curves of refrigerants by molecular simulation. *Fluid Phase Equilib.* **375**, 143–151 (2014). <https://doi.org/10.1016/j.fluid.2014.05.011>
48. J. Vrabec, G.K. Kedia, H. Hasse, Prediction of Joule–Thomson inversion curves for pure fluids and one mixture by molecular simulation. *Cryogenics* **45**, 253–258 (2005). <https://doi.org/10.1016/j.cryogenics.2004.10.006>
49. J. Vrabec, A. Kumar, H. Hasse, Joule–Thomson inversion curves of mixtures by molecular simulation in comparison to advanced equations of state: Natural gas as an example. *Fluid Phase Equilib.* **258**, 34–40 (2007). <https://doi.org/10.1016/j.fluid.2007.05.024>
50. J. Rößler, I. Antolovic, S. Stephan, J. Vrabec, Assessment of thermodynamic models via Joule–Thomson inversion. *Fluid Phase Equilib.* **556**, 113401 (2022). <https://doi.org/10.1016/j.fluid.2022.113401>
51. H. Renneis, S. Stephan, Characteristic curves of polar fluids: (I) the two-center Lennard–Jones plus dipole fluid. *Int. J. Thermophys.* (2024). <https://doi.org/10.1007/s10765-024-03366-8>
52. M. Urschel, S. Stephan, Determining Brown’s characteristic curves using molecular simulation. *J. Chem. Theory Comput.* **5**, 1537–1552 (2023). <https://doi.org/10.1021/acs.jctc.2c01102>
53. A. Batschinski, Abhandlungen über Zustandsgleichung; abh. I: Der orthometrische Zustand. *Ann. Phys.* **324**, 307–309 (1906)
54. M.C. Kutney, M.T. Reagan, K.A. Smith, J.W. Tester, D.R. Herschbach, The zero ($Z = 1$) behavior of equations of state: an interpretation across scales from macroscopic to molecular. *J. Phys. Chem. B* **104**, 9513–9525 (2000). <https://doi.org/10.1021/jp001344e>
55. E.M. Apfelbaum, V.S. Vorob’ev, G.A. Martynov, Triangle of liquid–gas states. *J. Phys. Chem. B* **110**, 8474–8480 (2006). <https://doi.org/10.1021/jp057327c>
56. E.M. Apfelbaum, V.S. Vorob’ev, G.A. Martynov, Regarding the theory of the Zeno line. *J. Phys. Chem. A* **112**, 6042–6044 (2008). <https://doi.org/10.1021/jp802999z>
57. K.S. Pitzer, Corresponding states for perfect liquids. *J. Chem. Phys.* **7**, 583–590 (1939). <https://doi.org/10.1063/1.1750496>
58. E.A. Guggenheim, The principle of corresponding states. *J. Chem. Phys.* **13**, 253–261 (1945). <https://doi.org/10.1063/1.1724033>
59. E.A. Guggenheim, C.J. Wormald, Systematic deviations from the principle of corresponding states. *J. Chem. Phys.* **42**, 3775–3780 (1965). <https://doi.org/10.1063/1.1695815>
60. J.H. Dymond, Corresponding states: a universal reduced potential energy function for spherical molecules. *J. Chem. Phys.* **54**, 3675–3681 (1971). <https://doi.org/10.1063/1.1675413>
61. S. Yang, J. Tian, H. Jiang, Corresponding-state principle model for the correlation of temperature dependent difference of coexisted densities of refrigerants at equilibrium. *Fluid Phase Equilib.* **560**, 113501 (2022). <https://doi.org/10.1016/j.fluid.2022.113501>
62. P. Orea, Y. Reyes-Mercado, Y. Duda, Some universal trends of the Mie(n, m) fluid thermodynamics. *Phys. Lett. A* **372**, 7024–7027 (2008). <https://doi.org/10.1016/j.physleta.2008.10.047>
63. E.A. Guggenheim, Corresponding states and surface tension. *Proc. Phys. Soc.* **85**, 811 (1965). <https://doi.org/10.1088/0370-1328/85/4/122>
64. I. Cachadina, A. Mulero, A new corresponding-states model for the correlation and prediction of the surface tension of organic acids. *Ind. Eng. Chem. Res.* **59**, 8496–8505 (2020). <https://doi.org/10.1021/acs.iecr.0c00832>
65. G. Galliero, M.M. Piñeiro, B. Mendiboure, C. Miqueu, T. Lafitte, D. Bessieres, Interfacial properties of the Mie $n=6$ fluid: molecular simulations and gradient theory results. *J. Chem. Phys.* **130**, 104704 (2009). <https://doi.org/10.1063/1.3085716>

66. J. Lenhard, S. Stephan, H. Hasse, A child of prediction. On the history, ontology, and computation of the Lennard–Jonesium. *Stud. Hist. Philos. Sci.* **103**, 105–113 (2024). <https://doi.org/10.1016/j.shpsa.2023.11.007>
67. S. Stephan, M. Thol, J. Vrabc, H. Hasse, Thermophysical properties of the Lennard–Jones fluid: database and data assessment. *J. Chem. Inf. Model.* **59**, 4248–4265 (2019). <https://doi.org/10.1021/acs.jcim.9b00620>
68. M. Kohns, S. Werth, M. Horsch, E. Harbou, H. Hasse, Molecular simulation study of the CO₂–N₂O analogy. *Fluid Phase Equilib.* **442**, 44–52 (2017). <https://doi.org/10.1016/j.fluid.2017.03.007>
69. R. Fingerhut, G. Guevara-Carrion, I. Nitzke, D. Saric, J. Marx, K. Langenbach, S. Prokopen, D. Celný, M. Bernreuther, S. Stephan, M. Kohns, H. Hasse, J. Vrabc, ms2: a molecular simulation tool for thermodynamic properties, release 4.0. *Comput. Phys. Commun.* **262**, 107860 (2021). <https://doi.org/10.1016/j.cpc.2021.107860>
70. G. Rutkai, A. Köster, G. Guevara-Carrion, T. Janzen, M. Schappals, C.W. Glass, M. Bernreuther, A. Wafai, S. Stephan, M. Kohns, S. Reiser, S. Deublein, M. Horsch, H. Hasse, J. Vrabc, ms2: a molecular simulation tool for thermodynamic properties, release 3.0. *Comput. Phys. Commun.* **221**, 343–351 (2017). <https://doi.org/10.1016/j.cpc.2017.07.025>
71. M. Lísal, K. Aim, M. Mecke, J. Fischer, Revised equation of state for two-center Lennard–Jones fluids. *Int. J. Thermophys.* **25**, 159–173 (2004). <https://doi.org/10.1023/B:IJOT.0000022332.12319.06>
72. L. Xu, Y.-Y. Duan, H.-T. Liu, Z. Yang, Empirical correlations for second virial coefficients of non-polar and polar fluids covering a wide temperature range. *Fluid Phase Equilib.* **539**, 113032 (2021). <https://doi.org/10.1016/j.fluid.2021.113032>
73. R. Lustig, Direct molecular NVT simulation of the isobaric heat capacity, speed of sound and Joule–Thomson coefficient. *Mol. Simul.* **37**, 457–465 (2011). <https://doi.org/10.1080/08927022.2011.552244>
74. R. Lustig, Statistical analogues for fundamental equation of state derivatives. *Mol. Phys.* **110**, 3041–3052 (2012). <https://doi.org/10.1080/00268976.2012.695032>
75. J. Gross, J. Vrabc, An equation-of-state contribution for polar components: dipolar molecules. *AIChE J.* **52**, 1194–1204 (2006). <https://doi.org/10.1002/aic.10683>
76. B.E. Poling, J.M. Prausnitz, J.P. O’Connell, *The Properties of Gases and Liquids*, 5th edn. (McGraw-Hill, New York, 2001)
77. S. Schmitt, H. Hasse, S. Stephan, Entropy scaling framework for transport properties using molecular-based equations of state. *J. Mol. Liq.* **395**, 123811 (2024). <https://doi.org/10.1016/j.molliq.2023.123811>
78. A. Mejía, C. Herdes, E.A. Müller, Force fields for coarse-grained molecular simulations from a corresponding states correlation. *Ind. Eng. Chem. Res.* **53**, 4131–4141 (2014). <https://doi.org/10.1021/ie404247e>
79. J. Jaramillo-Gutiérrez, J.L. López-Picón, J. Torres-Arenas, Subcritical and supercritical thermodynamic geometry of Mie fluids. *J. Mol. Liq.* **347**, 118395 (2022). <https://doi.org/10.1016/j.molliq.2021.118395>
80. P. Orea, A. Romero-Martinez, E. Basurto, C.A. Vargas, G. Odriozola, Corresponding states law for a generalized Lennard–Jones potential. *J. Chem. Phys.* **143**, 024504 (2015). <https://doi.org/10.1063/1.4926464>
81. A. Torres-Carbajal, L.A. Nicasio-Collazo, V.M.T. Montoya, P.E. Ramírez-González, Liquid–vapour phase diagram and surface tension of the Lennard–Jones core-softened fluid. *J. Mol. Liq.* **314**, 113539 (2020). <https://doi.org/10.1016/j.molliq.2020.113539>
82. P. Grosfils, J.F. Lutsko, Dependence of the liquid–vapor surface tension on the range of interaction: a test of the law of corresponding states. *J. Chem. Phys.* **130**, 054703 (2009). <https://doi.org/10.1063/1.3072156>
83. G.D. Fisher, T.W. Leland, Corresponding states principle using shape factors. *Ind. Eng. Chem. Fundam.* **9**, 537–544 (1970). <https://doi.org/10.1021/i160036a003>
84. G. Galliero, Surface tension of short flexible Lennard–Jones chains: corresponding states behavior. *J. Chem. Phys.* **133**, 074705 (2010). <https://doi.org/10.1063/1.3469860>
85. J.W. Leach, P.S. Chappellear, T.W. Leland, Use of molecular shape factors in vapor–liquid equilibrium calculations with the corresponding states principle. *AIChE J.* **14**, 568–576 (1968). <https://doi.org/10.1002/aic.690140407>
86. C. Vega, C. McBride, C. Mendiña, The second virial coefficient of the dipolar two center Lennard–Jones model. *Phys. Chem. Chem. Phys.* **4**, 3000–3007 (2002). <https://doi.org/10.1039/B200781A>

87. G.M. Kontogeorgis, D.P. Tassios, Critical constants and acentric factors for long-chain alkanes suitable for corresponding states applications. A critical review. *Chem. Eng. J.* **66**, 35–49 (1997). [https://doi.org/10.1016/s1385-8947\(96\)03146-4](https://doi.org/10.1016/s1385-8947(96)03146-4)
88. T. Holleman, Application of the principle of corresponding states to the excess volumes of liquid binary normal alkane mixtures. *Physica* **29**, 585–599 (1963). [https://doi.org/10.1016/s0031-8914\(63\)80217-7](https://doi.org/10.1016/s0031-8914(63)80217-7)
89. D. Fertig, S. Stephan, Influence of dispersive long-range interactions on transport and excess properties of simple mixtures. *Mol. Phys.* **121**, 2162993 (2023). <https://doi.org/10.1080/00268976.2022.2162993>
90. A. Galindo, L.A. Davies, A. Gil-Villgeas, G. Jackson, The thermodynamics of mixtures and the corresponding mixing rules in the SAFT-VR approach for potentials of variable range. *Mol. Phys.* **93**, 241–252 (1998). <https://doi.org/10.1080/002689798169249>
91. M. Lupkowski, P.A. Monson, Phase diagrams of interaction site fluids. *Mol. Phys.* **67**, 53–66 (1989). <https://doi.org/10.1080/00268978900100921>
92. M. Lísal, R. Budinský, V. Vacek, Vapour–liquid equilibria for dipolar two-centre Lennard–Jones fluids by Gibbs–Duhem integration. *Fluid Phase Equilib.* **135**, 193–207 (1997). [https://doi.org/10.1016/S0378-3812\(97\)00072-1](https://doi.org/10.1016/S0378-3812(97)00072-1)
93. J. Stoll, J. Vrabec, H. Hasse, Comprehensive study of the vapour–liquid equilibria of the pure two-centre Lennard–Jones plus point dipole fluid. *Fluid Phase Equilib.* **209**, 29–53 (2003). [https://doi.org/10.1016/S0378-3812\(03\)00074-8](https://doi.org/10.1016/S0378-3812(03)00074-8)

Publisher's Note Springer Nature remains neutral with regard to jurisdictional claims in published maps and institutional affiliations.